Supporting Information

Proton-Controlled Dzyaloshinskii–Moriya Interaction and Topological Hall Effect in Hydrogenated Strontium Ruthenate

Ya-Ting Xu[1#], Xu Niu[1#], Yi-Feng Zhao[1], Yu-Ke Zhang[1], Yu Cai[1], Meng-Yao Fu[1], Min Feng[1], Ke Qu[1], Xing Deng[1], Bo-Wen Wang[1], Ya-Qiong Wang[1], Zhao Guan[1], Zhen-Zhong Yang[1], Bin-Bin Chen[1], Ni Zhong[1,2]*, Chun-Gang Duan[1,2] and Ping-Hua Xiang[1,2]**

[1] Key Laboratory of Polar Materials and Devices (Ministry of Education), Shanghai Center of Brain-inspired Intelligent Materials and Devices, Department of Electronics, East China Normal University, Shanghai 200241, China.

[2] Collaborative Innovation Center of Extreme Optics, Shanxi University, Taiyuan, Shanxi 030006, China.

[#] Y.-T. X. and X.N. contributed equally to this work.

*E-mail: bbchen@phy.ecnu.edu.cn, nzhong@ee.ecnu.edu.cn, phxiang@ee.ecnu.edu.cn

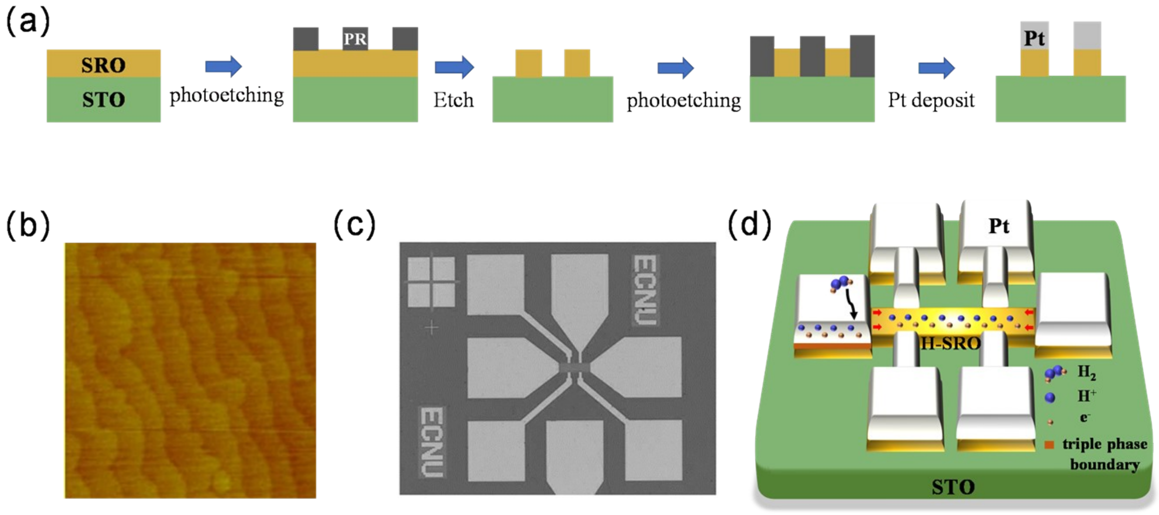

Figure S1. (a) A schematic representation of the manufacturing process for Hall effect devices (PR: Photoresist). (b) AFM image (1 μm×1 μm) of the surface morphology of SRO film. (c) Optical microscope image of the Hall bar structure. The channel size is 220×60 μm. (d) Schematic diagram of catalytic hydrogenation of platinum electrode.

As shown in Figure S1a, SRO films were patterned with Hall bar by photolithograph and argon-ion milling. Then, a Pt electrode with a thickness of 100 nm is printed on the SRO pattern through processes such as photolithography, magnetron sputtering, and lift off. Finally, the devices were placed in the hydrogen atmosphere to form an H-SRO via a Pt-assisted hydrogen spillover mechanism. Figure S1d schematically illustrates the proposed proton intercalation process in SRO thin films. At the triple phase boundary (Pt-SRO-H_2), H_2 first dissociates to atomic hydrogen and then splits to H^+ and e^-, which are incorporated into SRO lattice. Due to the hydrogen proton acting as an electron donor to provide electrons to the lattice, the electron transport and magnetic properties of H-SRO thin films have undergone significant changes. In addition, the insertion of protons induces small structural distortions in the SRO lattice, promoting the emergence of topological Hall effect. Please refer to the main text for specific details.

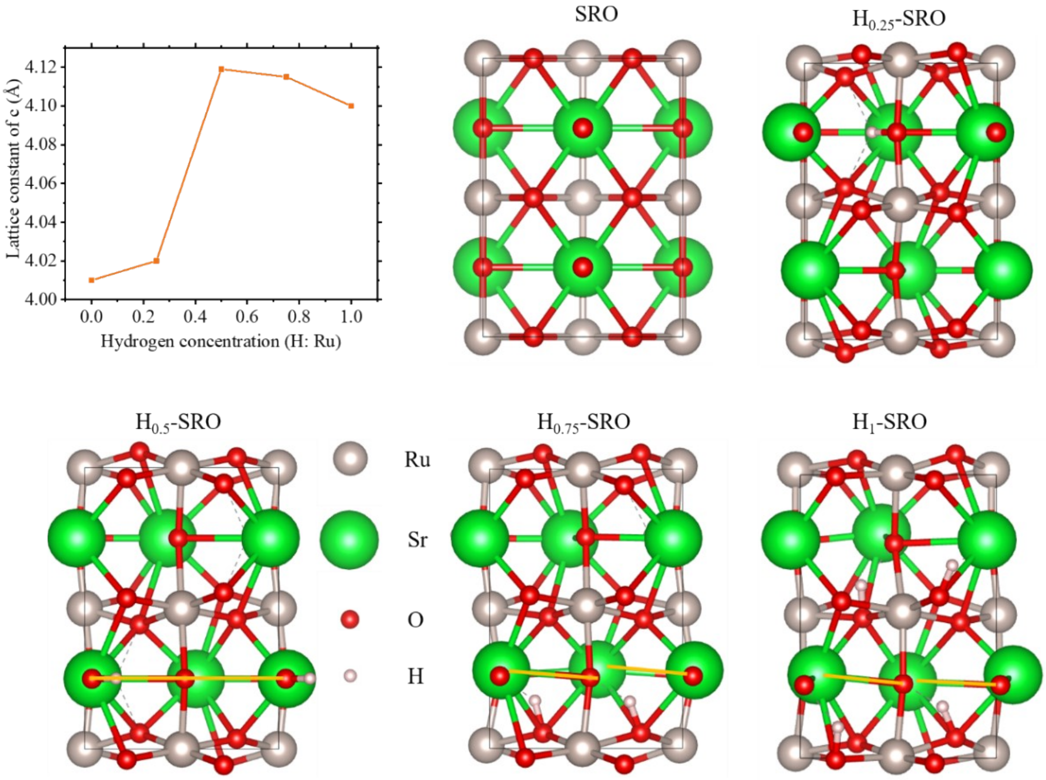

Figure S2. The variation of H-SRO out of plane lattice constant and crystal structure with H doping concentration.

In order to investigate the effect of H doping on the out-plane lattice constant, we fixed the in-plane lattice and relaxed it, obtaining the results shown in Figure S2. When the doping concentration is not high (less than 0.25 per unit cell), the lattice constant of SRO changes very little which is due to the displacement of oxygen atoms., This displacement offsets the lattice expansion that should have been caused by H doping. But when the concentration of hydrogen atoms increased to 0.5 per unit cell, this lattice expansion still occurred. As the hydrogen doping concentration further increases, the lattice constant expansion is once again suppressed by the distortion of the Sr-O plane. Based on the results of TEM, there is no distortion in the Sr-O plane, so the doping concentration of H dose not increase enough to cause lattice expansion.

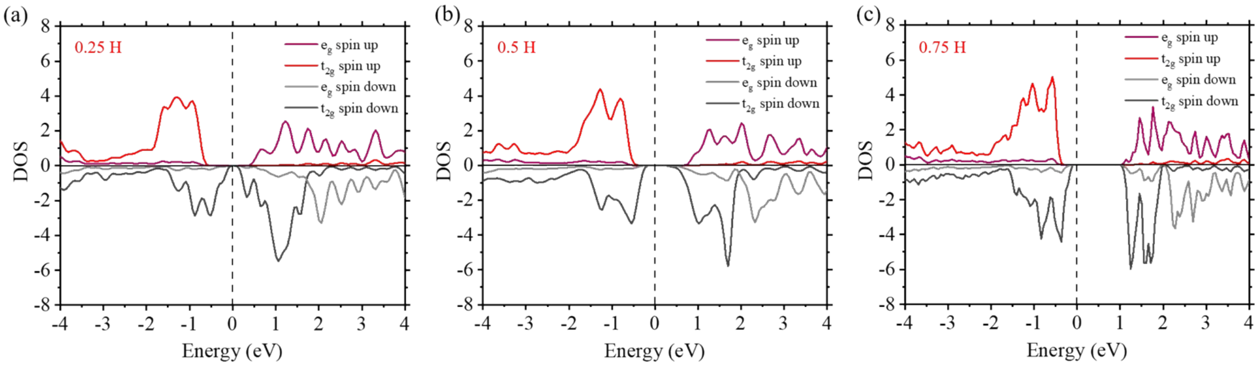

Figure S3. Density of state diagram of the SRO doped with 0.25 (a),0.5 (b) and (c)0.75 hydrogen per unit cell.

From Figures 3e and 3f in main text and Figure S3, it can be seen that as the hydrogen doping concentration in the SRO lattice increases, the band gap gradually increases. The conductivity of SRO gradually decreases with the increase of hydrogen doping concentration. Furthermore, it can be seen from the graph that as the hydrogen doping concentration increases, the difference between the majority of spin state electrons and the minority of spin state electrons gradually decreases, indicating that the magnetism of SRO weakens until the hydrogen doping concentration increases to 0.5 electrons per unit cell, and the magnetism is weaken. The results of the above theoretical calculations are consistent with the changes in the electrical transport and magnetic properties of SRO as the degree of hydrogenation increases, as measured in experiments.

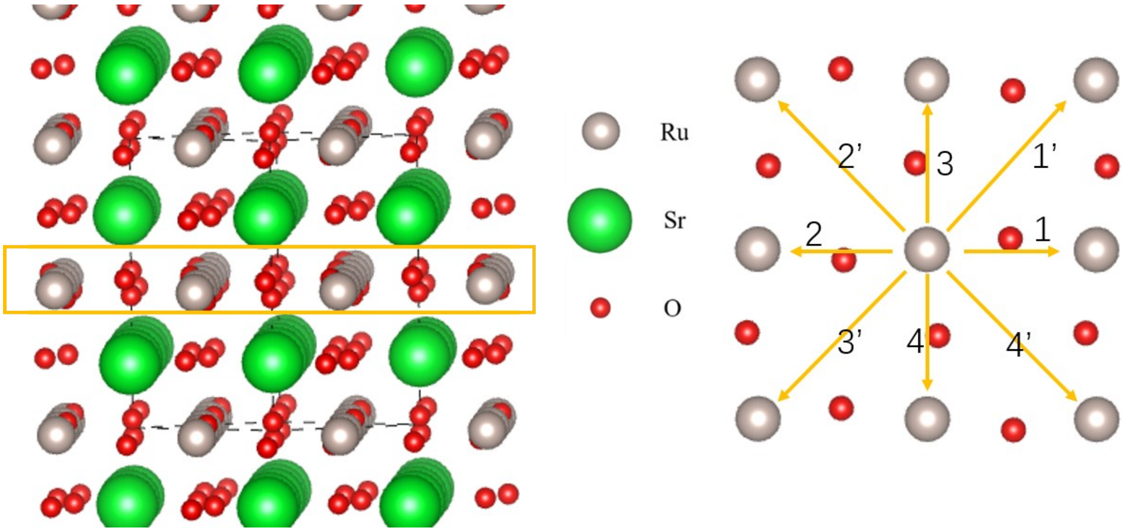

Figure S4. The schematic diagram of SRO unit cell. The top view inside the yellow box is placed on the right side. The yellow arrow represents the vector between the central Ru atom and the surrounding Ru atoms. Their corresponding magnetic exchange coefficients are given in **Table S1**.

Table S1. Heisenberg exchange coefficient J and DMI exchange coefficient D with different hydrogen doping concentrations. Nearest and next-nearest exchange parameter is given. All units are in meV.

		Jxx	Jyy	Jzz	Dx	Dy	Dz
Pure_SRO	1	5.05	5.00	3.66	0.21	-0.21	-0.02
	2	5.09	5.02	3.64	0.21	0.21	-0.02
	3	6.92	6.89	5.01	0.02	0.03	0.03
	4	6.85	6.82	4.92	-0.01	-0.01	-0.02
	1’	-5.17	-5.42	-6.25	0.01	-0.00	0.02
	2’	-5.30	-5.19	-6.19	-0.01	-0.02	-0.01
	3’	-5.17	-5.41	-6.25	-0.01	0.00	-0.02
	4’	-5.30	-5.19	-6.20	0.01	0.02	0.01
H0.25_SRO	1	-2.02	-1.47	-5.30	0.66	-0.83	-0.26
	2	-3.19	-3.32	-7.23	0.56	-0.87	-0.46
	3	0.49	-0.65	-0.83	-0.28	-0.39	0.46
	4	0.43	-0.70	-0.67	-0.26	-0.18	0.22
	1’	0.08	0.03	0.07	-0.01	0.00	0.00

	2’	-0.15	-0.17	-0.11	0.00	-0.01	-0.00
	3’	0.08	0.03	0.07	0.01	-0.00	-0.00
	4’	-0.15	-0.16	-0.11	-0.00	0.01	0.00
H0.5_SRO	1	-0.64	1.60	-0.43	-0.28	-0.25	0.11
	2	-0.62	1.61	-0.42	0.29	0.25	-0.10
	3	1.50	0.62	-0.28	0.62	-0.34	-0.31
	4	-1.40	0.58	-0.23	0.58	-0.32	-0.29
	1’	-0.11	-0.27	-0.00	0.00	0.00	0.00
	2’	-0.20	-0.55	-0.14	0.00	0.00	0.00
	3’	-0.06	0.09	-0.02	0.00	-0.00	-0.00
	4’	0.58	0.23	0.63	-0.00	-0.00	-0.00
H0.75_SRO	1	0.31	1.04	1.07	-0.15	0.15	0.13
	2	0.28	1.03	1.18	-0.12	0.14	0.17
	3	0.21	0.22	-0.23	0.21	-0.32	0.09
	4	0.36	0.68	0.09	0.31	-0.27	0.03
	1’	-0.10	-0.04	-0.07	0.01	0.01	-0.01
	2’	-0.13	-0.07	-0.05	-0.00	0.00	-0.00
	3’	-0.10	-0.04	-0.07	-0.00	-0.01	0.01
	4’	0.13	-0.07	-0.05	0.01	-0.00	-0.00
H1_SRO	1	-0.57	-0.74	0.14	0.47	-0.66	0.11
	2	-0.22	-0.40	0.36	0.41	-0.70	0.06
	3	-0.21	-0.21	-0.22	0.03	-0.02	-0.00
	4	-0.13	-0.15	-0.12	0.01	0.016	-0.02
	1’	-0.00	-0.00	-0.00	0.00	-0.00	-0.00
	2’	0.00	0.01	0.00	0.00	0.00	0.00
	3’	-0.01	-0.00	-0.00	0.00	0.00	0.00
	4’	-0.00	0.00	-0.00	-0.00	-0.00	0.00

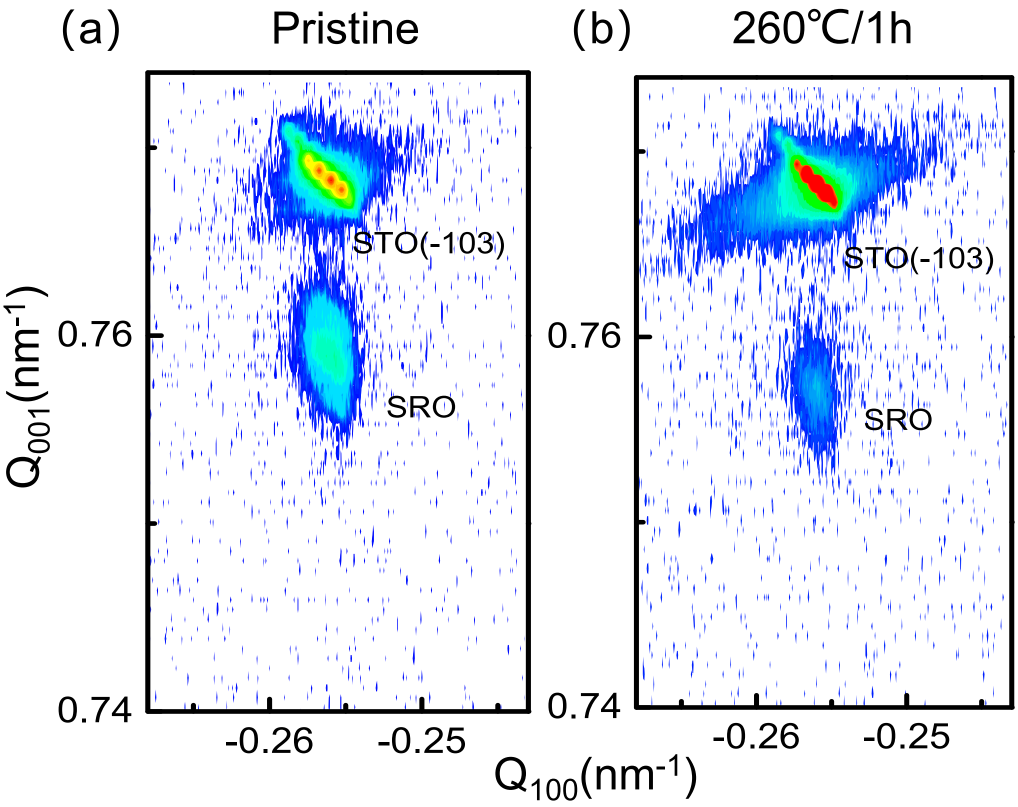

Figure S5. Reciprocal Space Mapping of the pristine SRO (a) and H-SRO hydrogenated at 260 °C(b) on the STO (-103) crystal plane.

In order to further characterize the changes of lattice parameters and epitaxial properties of SRO films before and after hydrogenation, reciprocal space mapping (RSM) measurements were carried out on the asymmetric crystal surface (-103) of pristine SRO and H-SRO hydrogenated at 260 °C. As shown in Figure S5, the RSM results show that the (-103) diffraction peak of the H-SRO is consistent with the X-axis of the (-103) peak of the STO substrate, indicating that the H-SRO thin films maintain coherent epitaxy with the substrate.

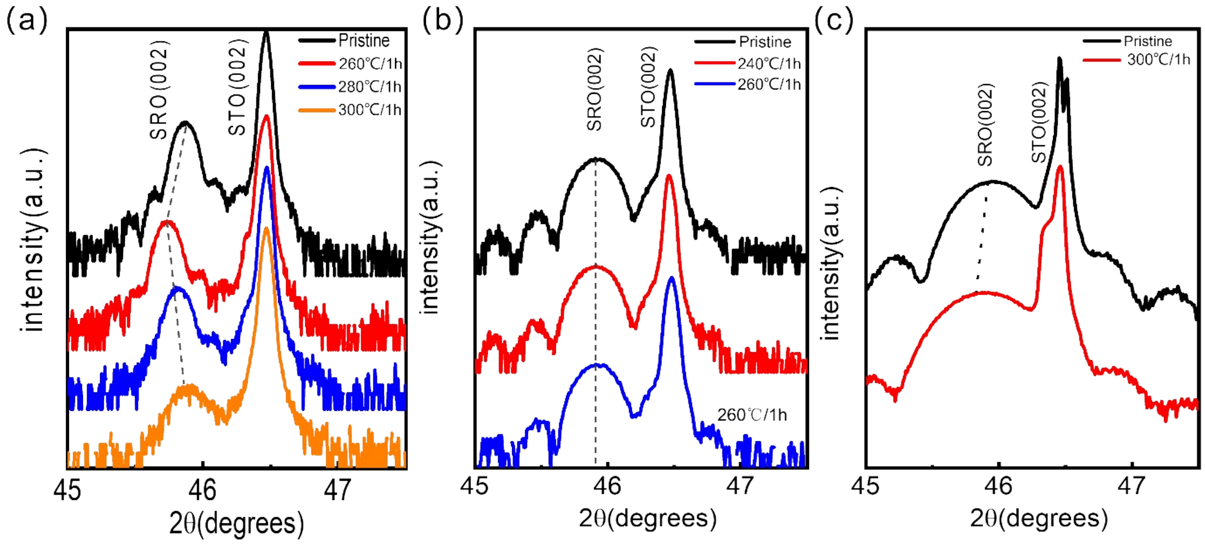

Figure S6. XRD θ-2θ scans of SRO film annealed in hydrogen atmosphere at different temperature (a) with Pt electrode, (b) and (c) without Pt electrodes.

Figure S6a investigated the effect of annealing temperature on hydrogenation efficiency. It is evident from the XRD pattern that increasing the temperature does not enhance the hydrogenation. On the contrary, when the temperature rises to 280 °C and 300 °C, the (002) diffraction peak of SRO no longer moves to the left, but returns to its initial position, which may be due to the increase in temperature causing the doped protons to leave SRO. Moreover, the diffraction peak of the SRO annealing at 300 °C is weakened compared to the initial film, indicating that excessive annealing temperature may lead to a decrease in the crystallinity of the SRO.

To determine whether the changes in the lattice structure of SRO are caused by proton doping, we annealed SRO thin films without Pt electrodes in a hydrogen atmosphere. Figure S4b shows the XRD pattern of the SRO without Pt electrodes hydrogenated under different conditions. The experimental results showed that without the catalytic effect of Pt electrode, the (002) diffraction peak of SRO dose not shift at all, indicating that the lattice structure of SRO has hardly changed when the annealing temperature is not higher than 260 °C. This can exclude the influence of other impurities such as oxygen vacancies that may be introduced during the annealing process. It can be confirmed that the slight lattice structure change of SRO in the hydrogenation experiment is due to the catalytic effect of Pt electrodes on proton doping.

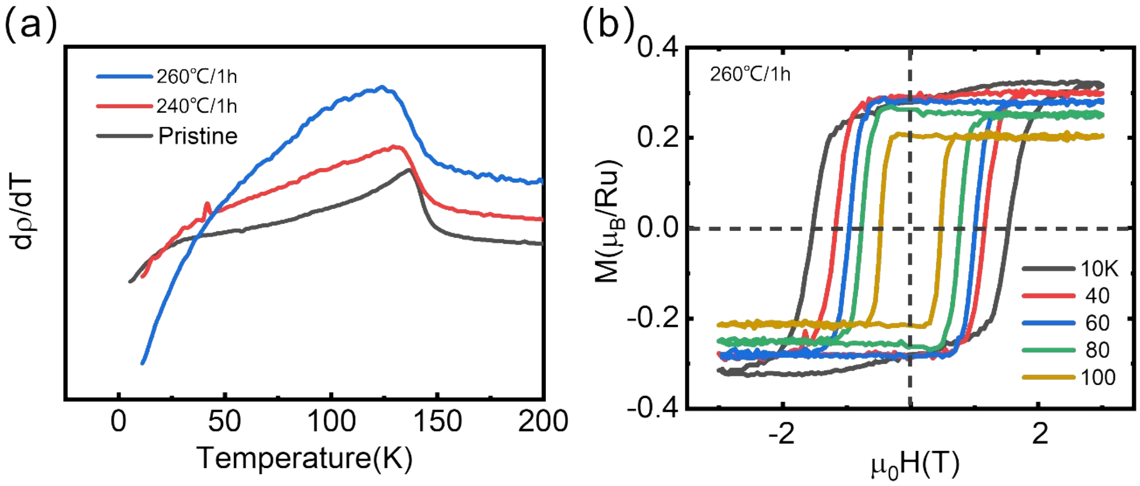

Figure S7. (a) Temperature derivative of ρ_{xx} of SRO and H-SRO thin films in Figure 2a. (b) Magnetic hysteresis loops of H-SRO hydrogenated at 260 °C at different temperatures.

As demonstrated in Figure S7a, the T_c can be derived from the resistivity curve. The findings suggest that as the hydrogenation temperature increases, T_c slightly decreases from 135 K to 130 K and then to 125 K. Figure S7b illustrates the magnetic hysteresis loop at temperatures ranging from 10 K to 100 K in the out-of-plane direction of the hydrogenated SRO thin films at 260 °C. The magnetization-temperature (*M-T*) curves of SRO thin films with varying degrees of hydrogenation, as shown in Figure 3c, and the magnetization-field (*M-H*) curves of SRO films hydrogenated at 260 °C, as depicted in Figure S7b, do not exhibit significant magnetic non-uniformity superposition. Consequently, the dual-channel AHE model can be disregarded. Upon further analysis and theoretical computations, we conclude that the hump feature observed in the Hall curve of proton-doped SRO films is primarily due to the emergence of intrinsic THE.

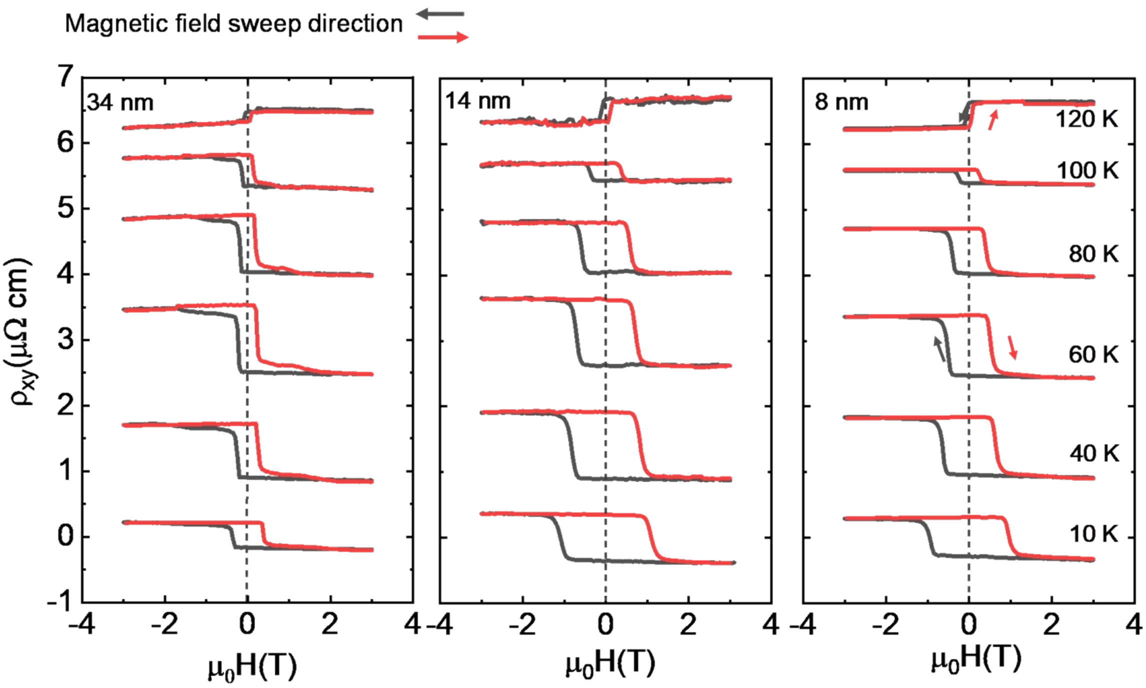

Figure S8. Magnetic field dependence of hall resistivity ρ_{xy} of SRO thin films with different thicknesses measured at various temperatures. The field sweeping directions are marked by arrows. The OHE component has been subtracted from all data sets in order to focus on the additional Hall effect.

Figure S8 illustrate the Hall resistivity of SRO thin films with thicknesses of 34 nm, 14 nm, and 8 nm as a function of magnetic field at temperatures ranging from 10 K to 120 K. The magnetic field is applied perpendicular to the sample surface, and the scanning range extends from -3 T to 3 T. To enhance the clarity of the AHE, the graph presents the data after subtracting the OHE contributions specific to each sample. Across all SRO samples, the Hall resistivity curve demonstrates hysteresis-like behavior indicative of typical ferromagnetic characteristics. The loop's AHE features suggest that the SRO film possesses strong vertical magnetic anisotropy. A consistent pattern emerges in the Hall resistivity curves: within the temperature interval of 100-120 K, the AHE signatures of all samples experience a transition. As depicted in Figures S6, below 100 K, the Hall resistivity of SRO samples follows a clockwise rotation with respect to the magnetic field; whereas at 120 K, it reverses to a counterclockwise direction.

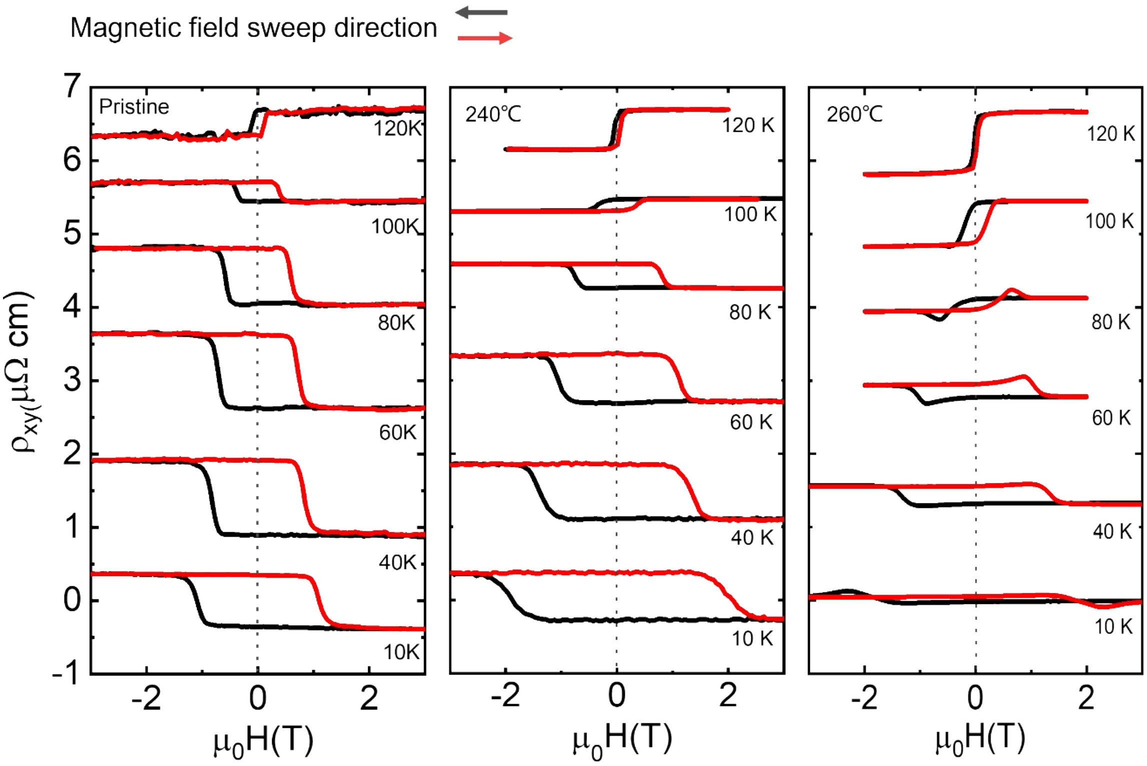

Figure S9. Magnetic field dependence of Hall resistivity ρ_{xy} for the 14-nm-thick pristine SRO and H-SRO hydrogenated at 240 °C and 260 °C measured at various temperatures. The field sweeping directions are marked by arrows. It should be noted that the OHE component has been subtracted from all data sets in order to focus on the additional Hall effect.

Figure S9 shows the magnetic field-dependent Hall resistivity ρ_{xy} of pristine SRO and H-SRO thin films over a temperature range from 10 K to 120 K. The Hall resistivity is measured by sweeping the magnetic field perpendicular to the film's surface. In the figure, the black and red curves represent different magnetic field sweep directions. It should be noted that the OHE component has been subtracted from all data sets in order to focus on the additional Hall effect. Both pristine SRO and the H-SRO hydrogenated at 240 °C show square hysteresis in their ρ_{xy}-μ_0H curve displays the characteristic AHE signatures, indicating significant perpendicular magnetic anisotropy. Notably, the temperature at which the AHE sign inverts is lower for the H-SRO hydrogenated at 240 °C than for pristine SRO. However, when the hydrogenating temperature increases to 260 °C, the pronounced hump-like features appear on the typical AHE hysteresis loops below 100 K.

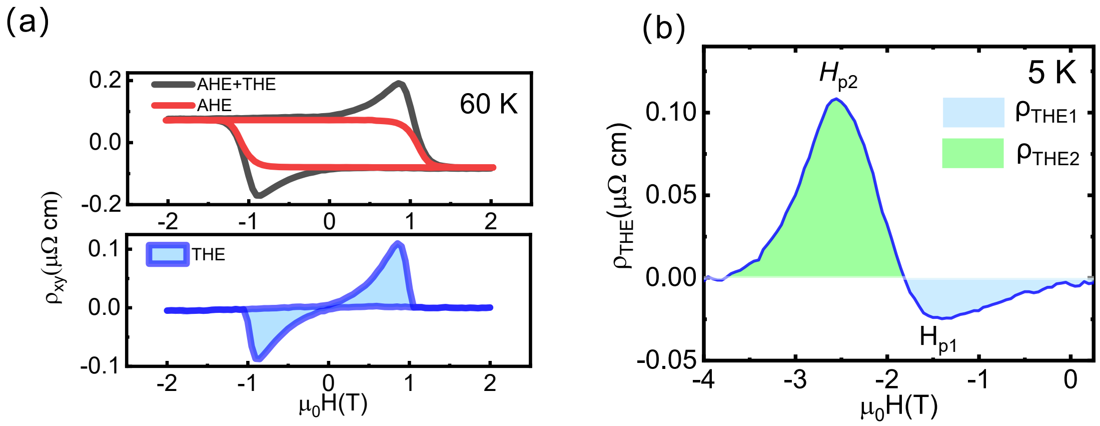

Figure S10. (a) Contributions of the AHE and the THE to the total Hall resistivity at 60 K for SRO thin film hydrogenated at 260°C. The OHE contribution is subtracted. (b) Hall resistivity at 5 K. The blue and green shaded regions indicate the contrasting signs of THE1 and THE2.

Figure S10 shows the characteristic results of the separation between AHE and THE at a temperature of 60 K, as observed in the Hall curve. As the magnetic field surpasses the critical value H_c, the influence of THE diminishes progressively until it becomes negligible. Consequently, the Hall resistivity is solely governed by the contributions from AHE and the eliminated OHE. The THE attains its maximum in a magnetic field of roughly ±0.85 T, suggesting that topological spin configurations associated with THE emerge predominantly around this particular magnetic field strength. When the temperatures is below 30 K, two typical THE signals occur. For the sake of clarity in our discussion, as shown in Figure S8b we consider the variation of the magnetic field from 0 T to -4 T as an illustrative example for the Hall measurement at 5 K. We designate the magnetic fields corresponding to the negative and positive maxima of ρ_{THE} as H_{p1} and H_{p2} respectively. Furthermore, we label the THE corresponding to the Hall resistivity curve and H_{p1} (below H_c) as ρ_{THE1} and the THE associated with H_{p2} (above H_c) as ρ_{THE2}.